Research Paper

Tumor Theranostics of Transition Metal Ions Loaded Polyaminopyrrole Nanoparticles

Shuyao Li[1], Shuwei Liu[1], Lu Wang[2], Min Lin[3✉], Rui Ge[1], Xing Li[2], Xue Zhang[1], Yi Liu[1], Lening Zhang[4✉], Hongchen Sun[1,2✉], Hao Zhang[1✉] and Bai Yang[1]

1. State Key Supramolecular Structure and Materials Laboratory, College of Chemistry, Jilin University, Changchun 130012, P. R. China;
2. The Oral Pathology Department, School and Hospital attached to Stomatology, Jilin University, Changchun 130021, P. R. China;
3. Collaborative Innovation Center attached to Marine Biomass Fibers, Shandong Province Materials and Textiles, Marine Biobased Materials Institute, Materials Science and Engineering School, Qingdao University, Qingdao 266071, P. R. China;
4. Department of Thoracic Surgery, China-Japan Union Hospital, Jilin University, Changchun 130033, P. R. China.

✉ Corresponding authors: Hao Zhang, PhD, State Key Supramolecular Structure and Materials Laboratory, College of Chemistry, Jilin University, Changchun 130012, P. R. China. Tel: +86 431 85159205; Email: hao_zhang@jlu.edu.cn. Hongchen Sun, PhD, The Oral Pathology Department, School and Hospital attached to Stomatology, Jilin University, Changchun 130021, P. R. China. Tel: +86 431 88796010; Email: hcsun@jlu.edu.cn. Min Lin, PhD, Collaborative Innovation Center attached to Marine Biomass Fibers, Shandong Province Materials and Textiles, Marine Biobased Materials Institute, Materials Science and Engineering School, Qingdao University, Qingdao 266071, P. R. China. Tel: +86 431 85159205; Email: linmin900401@126.com. Lening Zhang, PhD, Department of Thoracic Surgery, China-Japan Union Hospital, Jilin University, Changchun 130033, P. R. China. Tel: +86 431 85159205; Email: 951446482@qq.com.

Abstract

Polypyrrole (PPy) nanoparticles (NPs) possess high near-infrared absorption and good biosafety, showing the potentials as photothermal therapeutic materials. However, the single function and the weak diagnostic function limit the further combination with other functional units to achieve theranostics. In this work, polyaminopyrrole (PPy-NH$_2$) is demonstrated as the alternative of PPy for preparing NPs. Because of the amino group, metal ions, such as Cu(II) and Fe(III) can be loaded in PPy-NH$_2$ NPs, which extends the applications in multimodal theranostics. Systematical studies reveal that the contribution of Cu(II) in multimodal theranostics is greater than Fe(III). Cu can enhance T$_1$ response signal for magnetic resonance imaging (MRI) and be released controllably in the organism, leading to the effect of chemotherapy. Therefore, Cu(II) and Fe(III) co-loaded PPy-NH$_2$ NPs are defined as CuPPy-NH$_2$ NPs. Experimental results indicate that the optimal size of CuPPy-NH$_2$ NPs is 50.2 nm. The photothermal transduction efficiency is 76.4%. After thermochemotherapy, a complete ablation of human oral epithelial carcinoma tumors is observed. No tumor recurrence is found.

Methods: Cu(II) and Fe(III) co-loaded PPy-NH$_2$ NPs are prepared through oxidation polymerization by mixing Py-NH$_2$, CuCl$_2$, and FeCl$_3$ in water under stirring at room temperature, which are defined as CuPPy-NH$_2$ NPs. The as-prepared CuPPy-NH$_2$ NPs are tested with a variety of cell and animal experiments for tumor theranostics.

Results: CuPPy-NH$_2$ NPs have good light stability, photothermal stability, biosafety and low toxicity. The optimal size of theranostic CuPPy-NH$_2$ NPs is 50.2 nm, which present a photothermal transduction efficiency of 76.4%. The doped Cu(II) ions also show chemotherapeutic behavior. After thermochemotherapy, a complete ablation of human oral epithelial carcinoma tumors is observed. No tumor recurrence is found. Because of the unpaired electron in Cu atomic orbits, CuPPy-NH$_2$ NPs also show T$_1$-weighted magnetic resonance imaging.

Conclusions: This kind of transition metal-doped polymer gives a competitive approach for designing and fabricating multimodal theranostic nanodevices, which shows the potential in tumor treatment.

Key words: polyaminopyrrole nanoparticles, theranostics, magnetic resonance imaging, thermochemotherapy

Introduction

Tumor theranostics is a vitally significant application for nano-medical science [1-7]. Plenty of nanoplatforms, constructing from noble metal nanoparticles (NPs) [8-11], carbon-based materials [12-14], organic compounds [15, 16], polymers [17, 18] and some other inorganic NPs such as Fe_3O_4 [19, 20], SiO_2 [21-24], copper chalcogenides [25-27], are tested as novel agents for tumor diagnosis and combination therapies. Apart from these existing building blocks, transitional metal ions also exhibit theranostic functions [28-31]. For example, unpaired electrons in atomic orbits endow Mn(II), Co(II), Cu(II), Fe(III), and etc. as contrast agents for magnetic resonance imaging (MRI) [32-34], which is a precise and free of radiation imaging technique for the diagnosis of soft tissue lesion [35-38]. Some of the transitional metal ions also carry certain dosage of toxicity, which can be used as chemotherapeutic drugs for tumor treatment [39, 40]. Meanwhile, many transitional metal elements are essential to maintaining body health. Fe is crucial for the hemoglobins [41], Cu is important for blood stream formation [42], Zn influences hormonal level [43], and Co can be used for nerve repairing [44]. However, they are rarely exploited in tumor theranostics. The main hindrance is that metal ions cannot be directed injected in the form of salt or organic molecules chelated compounds. Metal cations can easily disturb the physiological equilibrium, change the activities of proteins and even induce severe toxicity, raising concerns for biosafety [45, 46].

Proper engineering arrangement is required for metal ions before medical applications. Biosafety polymer enveloping is a facile strategy and it has been used for the surface passion of NPs, increasing structural stability as well as surface passivation and reducing toxicity from releasing [47]. One of the frequently used polymers is polypyrrole (PPy) due to the easy fabrication. PPy is a conductive polymer with good biosafety and it is widely used as covering material of Au-based nanomaterials, SiO_2 NPs and some supramolecular structures [8, 22]. Additionally, Liu et al. reported pure PPy NPs as sufficient heat generator under NIR laser irradiation for the effective photothermal ablation of malignant tumors [48]. However, PPy NPs still show limitation in several aspects. First, the function of tumor diagnosis should be included. Second, appropriate method is required to track and identify PPy NPs *in vivo*. Thirdly, though Zhen and his colleges revealed the biodistribution of SiO_2@PPy [49], the accumulation of pure PPy NPs in vital organs and tumor needs detailed study for the full estimation after systemic injection. Hence, properly engineered metal ions in PPy NPs would solve aforementioned aspects perfectly. On the one hand, by importing imaging capability from metal ions, PPy NPs can achieve tumor diagnosis and therapy simultaneously [50]. On the other hand, metal elements labeling PPy can provide the feasibility to monitor the change of PPy concentration *in vivo* through MRI, such as in blood, brain, muscles, and inner visceral organs [51-53].

The tumor theranostic performance is also affected by the doping quantity of metal ions, while the monomer pyrrole (Py) is of low coordination capability to metal ions, resulting into low loading capability of PPy NPs. Moreover, when chemotherapeutic metal ions is loaded, the weak coordination interaction between metal ions and PPy carriers may break up in normal physical conditions, causing damages to normal tissue [54, 55]. Hence, stronger coordination bonding is required to improve the metal ion loading efficiency and the biosafety. In this work, we replace Py with Py-NH_2 to increase the coordinative ability with transitional metal elements. Thus, Cu(II) and Fe(III) are loaded in PPy-NH_2 (CuPPy-NH_2) NPs during the polymerization. Both Cu(II) and Fe(III) can equip PPy-NH_2 NPs with MRI tumor diagnosis [39, 56]. Besides, Cu(II) can also label PPy-NH_2 NPs and make the NPs traceable in blood and vital organs [57, 58]. After CuPPy-NH_2 NPs reach cancerous area based on the enhance permeability and retention (EPR) effect, Cu(II) can be released from NPs and exhibit chemotherapeutic behavior [9]. The onefold tumor inhibition rate for chemotherapy is 70.6 %. Further combining photothermal therapy, the thermochemotherapy can completely ablate tumors without recurrence. The biosafety of CuPPy-NH_2 NPs is also carefully explored and the results indicate that CuPPy-NH_2 NPs are safe and of high performance in tumor theranostics.

Methods

Materials

All the reagents were commercially available products and used directly without further purification. Deionized water was used directly in all experiments. Propidium iodide (PI) and fluorescein diacetate (FDA) were purchased from Invitrogen. 1-Aminopyrrole (Py-NH_2, >98.0%) was purchased from Tokyo Chemical Industry. Ferric trichloride-hexahydrate ($FeCl_3·6H_2O$), copper chloride dehydrate ($CuCl_2·2H_2O$), 3-(4,5-dimethyl-2-thiazolyl)-2,5-diphenyl-2-H-tetrazoliumbromide (MTT), mercaptoethylamine (MA, 99+%), mercaptoglycerol, 3-mercaptopropionic acid (MPA, 99+%) and glutathione (GSH, 99%) were got in Sigma-Aldrich. Ammonium hydroxide ($NH_3·H_2O$, 25%) was purchased from Beijing Chemical Works.

Preparation of CuPPy-NH₂, PPy-NH₂ and Cu-loaded polypyrrole NPs

CuPPy-NH₂ NPs were prepared by mixing 0.5 mmol Py-NH₂, 1 mmol CuCl₂, and 4 mmol FeCl₃ in 120 mL water under stirring at room temperature for 24 h. By reducing the dosage of Fe(III) from 4.0 to 3.5, 3 and 2.5 mmol, the diameter of CuPPy-NH₂ NPs are adjustable from 50.2 ± 5.0 to 20.3 ± 3.0 nm. Through the similar method, PPy-NH₂ and Cu-loaded polypyrrole (CuPPy) NPs were also prepared. The products were collected after high speed centrifugation for 20 min under 2000 rcf (g's). The NPs were dispersed in deionized water for further tests and characterizations.

Metal ion release

5 mg/mL CuPPy-NH₂ NPs aqueous solution were mixed with 10 mM ammonia (-NH₂), sodium citrate (-COOH) and mercaptoglycerol (-SH), respectively. At different time intervals, through high speed centrifugation the CuPPy-NH₂ NPs were discarded. The released dose of ions in supernatant was determined by inductive coupled plasma atomic emission spectrometer (ICP-AES).

Cytotoxicity test and the photothermal effect *in vitro*

The human oral epithelial carcinoma (KB) cells were incubated with different concentrations of CuPPy-NH₂ NPs. After 24 h in standard cell media, the cell viability for KB cells was determined by a standard MTT assay on 96-well plates. The MTT test was measured by the optical density (OD) at 490 nm. As for the *in vitro* of photothermal therapy, KB cells were incubated with the concentration of 50 µg/mL CuPPy-NH₂ NPs for 30 min. Then each sample was irradiated at different power densities by an 808 nm NIR laser for 8 min. As for the control group, cell viability was tested at the same conditions without adding CuPPy-NH₂ NPs. Each experiment was repeated for five times.

PI and FDA co-staining assay

The treatment efficacy was revealed by PI and FDA. 30000 KB cells were seeded in a 12-well plate. The KB cells were incubated for 30 min with the concentration of 50 µg/mL CuPPy-NH₂ NPs containing 100 µg/mL of GSH in cell culture and incubated with cells. Each plate was irradiated at 0.33 W/cm² for 0, 3, 8, and 10 min, respectively, by an 808 nm laser. After that, 1 µg/mL PI and FDA were added into the KB cell culture in sequence with incubation for 15 min and 30 s, respectively. Finally, fluorescent photographs were taken under the excitation of 488 and 543 nm, respectively.

Animal experiments

4-6 weeks' old balb/c. nude (weighing ~18g) were purchased from Beijing Huafukang Biological Technology Co. Ltd. The mice were used under protocols approved by Jilin University Laboratory Animal Center. After one week's observation, their weights got a basic normal value around 19 g. 1.5×10^6 of KB cells dispersed in 100 µL of cell culture were injected subcutaneously into the right back leg of the mice. The tumor size was measured by a digital caliper every day. When the average tumor size reached ~100 mm³, the mice were allocated into four groups: control group, laser only group, chemotherapy (CuPPy-NH₂ NPs only) group, and thermo-chemotherapy (laser + CuPPy-NH₂ NPs) group. Moreover, the mice were administrated with CuPPy-NH₂ NPs by intravenous (i.v.) injection. The chemotherapy group and thermo-chemotherapy group were injected with 50 µL 1 mg/mL CuPPy-NH₂ NPs. And as for the control group and laser only group were intravenously injected with same volume of saline. The tumors in laser only and thermo-chemotherapy group were irradiated for 20 min by an 808 nm laser at 0.33 W/cm² two days after injection. In addition, the sizes of the tumor and the weights of the mouse were measured every other day. The tumor volume was calculated by the following formula:

$$V = 1/2 \cdot L \cdot D^2$$

(L (mm) = the tumor sizes in long axes; D (mm) = the tumor sizes in short axes). After CuPPy-NH₂ NPs injection for 16 days, the tumors of the treatment groups and the control group above were taken for further experiments: surgery, weighted by a scale and taken photos through a camera. The tumors and major organs and tissues (lungs, liver, heart, spleen, and kidneys) from each group were taken after heart perfusion and they were also soaked with formalin for further hematoxylin-eosin (H&E) staining.

Blood circulation and biodistribution

For blood circulation of CuPPy-NH₂ NPs, the same dose of blood (8 µL) was collected from each mouse at different time intervals and then dissolved in chloroazotic acid (HCl/HNO₃ = 3:1). And the mixed solution was analyzed by ICP-AES to determine the total amount of Cu in the blood. Major organs and tissues (liver, spleen, kidneys and tumor) from balb/c. nude (n=8) were collected at the indicated time point to demonstrate the CuPPy-NH₂ NPs biodistribution.

MRI study *in vivo*

The mice were planted with one tumor in the right side of the back legs. Each mouse was

intravenously injected with 50 µL 1 mg/mL of $CuPPy-NH_2$ NPs. 24 h later, the mice were anaesthetized and imaged under 1.5 T magnetic field.

Characterization

The UV-visible (UV-vis) absorption spectrum was recorded using a UV-3600 UV-vis spectrophotometer. Transmission electron microscopy (TEM) was characterized by a Hitachi H-800 electron microscope. The Dynamic light scattering (DLS) measurements were implemented using Zetasizer NanoZS (Malvern Instruments). The tests above were all conducted at room temperature. The infrared thermal images photos were taken by FLUKE infrared Ray (IR) thermal camera. The concentration of Cu was measured by ICP-AES. VG ESCALAB MKII spectrometer with an Mg Kα excitation (1253.6 eV) was used to perform X-ray photoelectron spectroscopy (XPS) investigation.

Results and Discussion

In our experiment, Cu(II) and Fe(III) chelated $PPy-NH_2$ ($CuPPy-NH_2$) NPs are prepared through oxidative polymerization. By changing the initiating concentration of Fe(III), the obtained NPs are quasi-spherical with the adjustable diameters from 50.2 ± 5.0 to 20.3 ± 3.0 nm (Figure 1A-D). High concentration of Fe(III) is used to initial the oxidative polymerization of $Py-NH_2$, where the molar ratio of Fe(III) to $Py-NH_2$ is 5~8:1. The excessive Fe(III) in the reaction plays three roles, namely, improving the loading quantity of Fe(III) in $PPy-NH_2$ NPs, ensuring the complete polymerization of $Py-NH_2$ and providing good colloidal stability. In aqueous solution, PPy NPs are conventional prepared in polymer stabilizers like poly (vinyl alcohol) considering the easy aggregation for pure PPy NPs [48]. But in our system, Fe(III) gives the essential surface potentials for $PPy-NH_2$ NPs (+ 19 mV) by ionization, which provides the critical electrostatic repulsions among NPs without protonating amino groups. Further increasing the feeding ratio of Fe(III) to $Py-NH_2$ above 9:1, the sizes of NPs would not grow larger than 50 nm because of the fast consumption of monomer (Figure S1). Cu(II) is also loaded during the polymerization under competitive coordination with Fe(III). The loading Cu(II) could hardly change the quasi-spherical morphology and the size of $PPy-NH_2$ NPs (Figure S2A). However, the light absorption is enhanced in large scale from visible to near-infrared (NIR) region after the loading of Cu(II) (Figure 1E). As for the NPs of 50.2, 49.8 nm, light extinction coefficient at 808 nm is 4.90×10^8 and 3.04×10^8 $M^{-1}cm^{-1}$ with and without chelating Cu(II) (Figure 1F). The enhancement of light absorption results from the vis-NIR light extinction ability of cupreous complexes [10, 39]. When amino groups coordinate Cu(II), the complexes exhibit enhanced absorption peak from 0.6 to 0.8 (Figure S3). In addition, the size of NPs also affects the light extinction capability (Figure 1E, F, S4). The light extinction coefficients are 4.22×10^8, 4.43×10^8, 4.67×10^8 and 4.90×10^8 $M^{-1}s^{-1}$ for the $CuPPy-NH_2$ NPs of 20.3, 31.4, 43.2 and 50.2 nm, respectively.

The structural information of $CuPPy-NH_2$ NPs is further revealed by XPS. The Fe: Cu ratio of 4:1 is chosen to make the CuPPy-NH2 NPs. As shown in Figure 2, the binding energy of N shows the linkage of N-H, N-Cu and N-Fe at 399.7, 400.7 and 401.2 eV, respectively [59]. In addition, the binding energy of Cu also reveals the linkage of Cu-O and Cu-Cl (Figure 2B) [60], which results from the hydration water and counterions of Cl (Figure 2C) [61]. By comparison, the N spectrum of $PPy-NH_2$ NPs without chelating Cu(II) only shows the linkage of N-H and N-Fe at 399.6, 401.0 eV (Figure S5A) [59]. Moreover, Cu is not covalently bound to PPy NPs. But a slight Cu can still adsorb on PPy NPs, despite the content of Cu is only 0.7%. Due to the low coordinating capability of Py, we could hardly observe the linkage of N-metal from the CuPPy NPs, and the content of Cu(II) cannot be improved in CuPPy NPs (Figure S5A and B). Further combining the ICP-AES data, the formula of $CuPPy-NH_2$ NPs and $PPy-NH_2$ NPs are speculated as
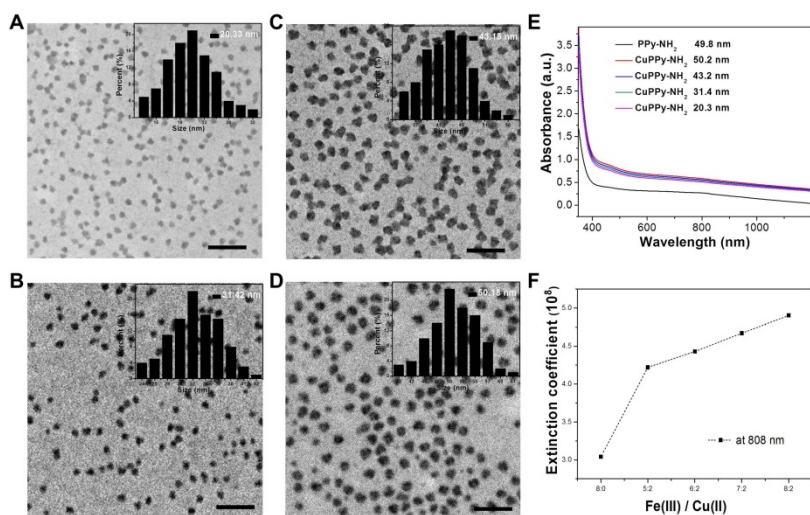

Figure 1. TEM images of the as-prepared $CuPPy-NH_2$ NPs with the diameter of 20.3 ± 3.0 (A), 31.4 ± 8.0 (B), 43.2 ± 4.0 (C), and 50.2 ± 2.0 nm (D). The scale bar in (A)-(D) represents 200 nm. (E) UV-vis absorption spectra of the as-prepared $PPy-NH_2$ and $CuPPy-NH_2$ NPs with different diameter. (F) The light extinction coefficients of $CuPPy-NH_2$ NPs at 808 nm.

$[C_4N_2H_4(CuCl_2)_{0.6} \cdot (H_2O)_{0.2}(FeCl_3)_{0.17}]_n$ and $[C_4N_2H_4(FeCl_3)_{0.22}]_n$, respectively.

The loading of Cu(II) improves the photothermal performance of PPy-NH$_2$ NPs. As shown in Figure 3, the temperature of aqueous solution containing NPs exhibits dramatic increments while irradiated by an 808 nm laser. When the laser power density is set at 3.5 W/cm^2, the increment in temperature is 47.4 °C for CuPPy-NH$_2$ NPs after 20 min irradiation, while it is only 26.2 °C for PPy-NH$_2$ without loading Cu(II) (Figure 3A). The temperature increment is also affected by the size of CuPPy-NH$_2$ NPs, since larger NPs possess higher light extinction capability (Figure 1E) [8]. As shown in Figure 3B, the NPs of 50 nm exhibit the best photothermal performance. Within 20 min irradiation, the temperature increment for 50 nm is 3 °C higher than that of 20 nm (Figure 3B). Besides, the photothermal converting performance is also influenced by the laser power densities and NPs concentrations (Figure 3C and D). When larger sum of NIR light or higher concentration of NPs is applied, the temperature increment is also higher because of collective heating effect [48]. We additionally determined the photothermal transduction efficiency (η) of CuPPy-NH$_2$ NPs, which represents the heat converting efficiency from absorbed light. By recording the real-time temperature of aqueous solution containing CuPPy-NH$_2$ NPs during the heating and cooling procedure, the η of CuPPy-NH$_2$ NPs is calculated as 76.4 %, while it is only 54.0 % for PPy-NH$_2$ NPs without loading Cu(II) (Figure S6). These evidences confirm that Cu(II) is the main contributor to the enhancement of photothermal performance. It should be noted that considering the DLS diameter of 50 nm NPs is 98.0 nm (Figure S7). The real size of NPs may be between TEM observation and DLS measurement in biological experiments because of the complex physiological environment. As reported, the NPs with diameters of 10-100 nm are most suitable for tumor theranostics applications. The CuPPy-NH$_2$ NPs of 50.2 nm is exploited in the following theranostic performance tests.

Since Fe(III) and Cu(II) possess unpaired electrons in the atomic orbits, they can shorten the longitudinal relaxation (T$_1$) of surrounding protons in high-energy of magnetic fields [25, 39]. As revealed in concentration dependent T$_1$-weighted MRI images (Figure 4B), both Cu(II) and Fe(III) could lighten up water under 1.5T magnetic field. And the respective relaxation rate (r$_1$) of Cu(II) and Fe(III) is 0.21 and 0.70 mM^{-1}s^{-1} as determined by a 500 M nuclear magnetic resonance (NMR) spectrometer (Figure 4A). The loading Fe(III) and Cu(II) would endow the CuPPy-NH$_2$ NPs with enhanced contrasting performance in MRI. CuPPy-NH$_2$ NPs exhibit continuous enhancement of MRI signals with increasing concentrations (Figure 4B). The r$_1$ is tested as 4.72 mM^{-1}s^{-1} based on the concentration of Cu(II) (Figure 4A), which is higher than clinical used Gd complexes (4.25 mM^{-1}s^{-1}).

The theranostic performance of CuPPy-NH$_2$ NPs is tested with cancerous cells *in vitro*. KB cells are chosen to evaluate the photothermal ablation efficiency of CuPPy-NH$_2$ NPs. Before incubating CuPPy-NH$_2$ NPs with KB cells, the colloidal stability is first tested towards different physical environment including water, saline, PBS, cell culture with and without serum (Figure 5A). After storage for 7 days, no obvious aggregation is found in all of the solutions except for PBS. However, the aggregated CuPPy-NH$_2$ NPs could be redispersed in PBS for more than 20 h after shaking (Figure S8), which would not hinder the following applications *in vitro* and *in vivo*. Besides, CuPPy-NH$_2$ NPs also exhibit good structural stability under laser irradiation. As shown in Figure 5B, the CuPPy-NH$_2$ NPs remain good NIR photothermal converting capability after five cycles of heating up to 80 °C and cooling down to room temperature. The absorption spectrum also confirms that no obvious change happens after irradiated with higher laser energy (Figure 5C).
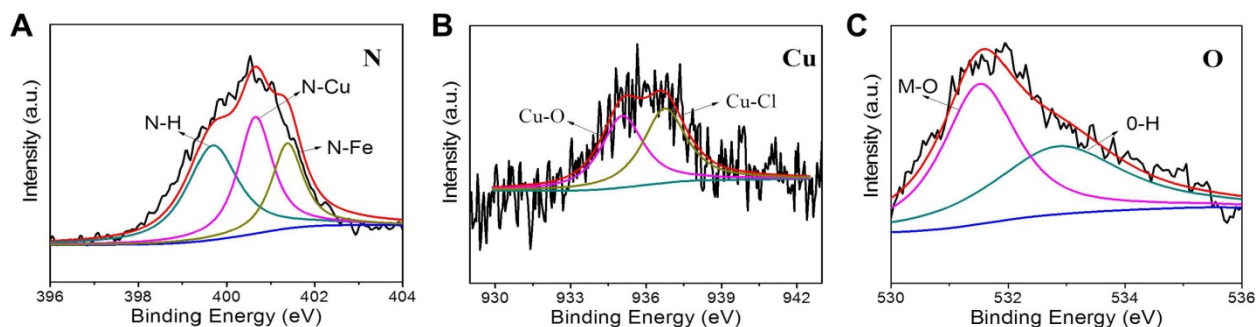

Figure 2. XPS N 1s (A), Cu 2p$_{3/2}$ (B), and O 1s (C) spectra of the as-prepared CuPPy-NH$_2$ NPs.

Then, CuPPy-NH$_2$ NPs and PPy-NH$_2$ NPs are incubated with KB cell at various concentrations for 24 h to evaluate the cytotoxicity. As revealed in Figure 6A, when the feeding concentration is below 100 μg/mL, CuPPy-NH$_2$ NPs could hardly cause any damages to the KB cells and the relative cell viability is high than 95 %. Further increasing the concentration to 200 μg/mL, the cell viability remains 81 %. However, when the concentration reaches 400 μg/mL, only 58 % of the KB cells survived after 24 h, which may result from toxic component of Cu(II). The PPy-NH2 NPs have no obvious damage to KB cells, representing the low cytotoxicity. Hence, in the following photothermal ablation of KB cells, the incubation concentration of CuPPy-NH$_2$ NPs is set at 50 μg/mL to avoid the toxicity caused cell damages. After irradiated by the 808 nm laser for 8 min, the cell viability decreases with growing laser power densities. When the power density increases to 1.8 W/cm^2, nearly 50 % of the KB cells are ablated to apoptosis (Figure 6B). Continuously increasing the laser power density to 3 W/cm^2, the majority of KB cells are dead and the cell viability decreases to 27 %. By comparison, the KB cells without incubation with CuPPy-NH$_2$ NPs could hardly receive any damages after the same dosage of irradiation. Besides, the apoptotic cells after laser irradiation are further stained by FDA and PI (Figure 6C-F). FDA could only stain living cells with green fluorescence while PI could only stain apoptotic cells into red fluorescence. As exposed under laser irradiation for 0, 2, 4, 8 min, the fluorescent images clearly exhibit that the green fluorescence is gradually replaced by red (Figure 6C-F), indicating the growing number of apoptotic cells. These evidences confirm that CuPPy-NH$_2$ NPs can effectively ablate KB cells under the 808 nm laser irradiation.

After *in vitro* tests, *in vivo* experiments are further performed to evaluate the potentials in tumor diagnosis and therapies. CuPPy-NH$_2$ NPs are i.v. injected into mouse bearing KB tumors. 24 h after injection, liver and renal functions are tested to reveal the short term safety of NPs. As shown in Figure S9, the injection of CuPPy-NH$_2$ NPs could hardly disturb the normal functions. Besides, MRI test is applied to trace the distribution of CuPPy-NH$_2$ NPs in tissues and organs (Figure 7). Comparing with blanket controls, the mice injected with NPs exhibit enhanced MRI signals in heart, lungs, kidneys, spleen and liver, as well as other tissues like muscles and lymphs. The NPs are mainly consumed by liver and kidneys, and the accumulation rate is 10.2 and 12.0 injected dose per gram tissue (% ID/g) (Figure 7A). It should be noted that the accumulation of NPs in tumor area is also significant, which favor the diagnosis of tumor. The tumor size, shape and edges are clearly shown in T$_1$-weighted MRI images (Figure 7F). As determined by ICP-AES, the KB tumor uptake rate is 5.7 %ID/g.
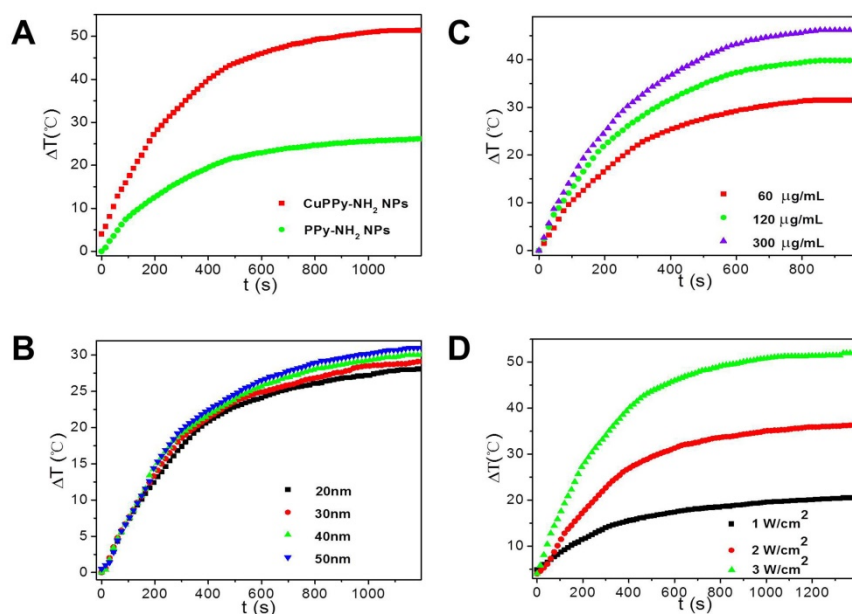
In addition to tumor diagnosis

Figure 3. (A) The temperature increment of PPy-NH$_2$ and CuPPy-NH$_2$ NPs. 1 mg/mL NPs are irradiated by a 3.5 W/cm^2 808 nm laser. (B) The temperature increment of CuPPy-NH$_2$ NPs in different sizes. 100 μg/mL NPs are irradiated by a 3.5 W/cm^2 808 nm laser. (C) The temperature increment of CuPPy-NH$_2$ NPs under different concentration. 50 nm NPs are tests by 3.5 W/cm^2 808 nm laser. (D) The temperature increment of CuPPy-NH$_2$ NPs with different power density of the 808 nm laser. 1 mg/mL 50 nm CuPPy-NH$_2$ NPs are used.
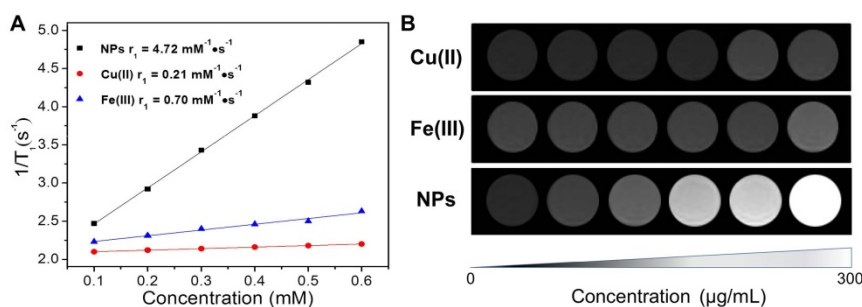

Figure 4. (A) Transverse relaxation time (T$_1$) relaxation rates (r$_1$) for CuPPy-NH$_2$ NPs, Cu(II) and Fe(III). (B) The concentration-dependent T$_1$-weighted MRI under 1.5 T magnetic field for CuPPy-NH$_2$ NPs, Cu(II) and Fe(III).

in MRI, the CuPPy-NH$_2$ NPs remained in tumor tissue could also perform combination tumor therapies. KB tumor is a fast growing malignant tumor, and the tumors in control group can expand from 100 to more than 2200 mm^3 within 16 days without any depressions (Figure 8A and C). When an 808 nm laser is applied to irradiate the tumors without NPs injection at the power density of 0.33 W/cm^2, the tumors could hardly observe any damages based on the observation of H&E stained tumor slices, and the average tumor volume could reach more than 2000 mm^3 (Figure 8A, D, S10). However, the tumors receive i.v. injection of CuPPy-NH$_2$ NPs exhibit an obvious depression in size, which is attributed from the release of chemotherapeutic Cu(II) (Figure 8A, E). In order to reveal the metal ion release mechanism, we incubate CuPPy-NH$_2$ NPs in various environments containing different functional groups including the -SH, -COOH and -NH$_2$ for 24 h (Figure S11A) [62, 63]. The results show that the released quantity of Cu(II) is the highest in -SH, which may contribute from the strong coordination interactions with –SH [26]. In addition, the release of Cu from the NPs in serum is 3.5% (Figure S12). This indicates that Cu is stable in serum. Since the microenvironment of tumor is acid and rich of GSH, Cu(II) is more likely to release from the carriers after CuPPy-NH$_2$ NPs reaching the tumor area, thus generating chemotherapeutic effects for KB tumors. As observed from the H&E stained tumor slices, the locally damaged tumor tissue with broken cells and vanishing nuclear is the direct factor tumor depressions, and the tumor inhibition rate is 70.6 % comparing with the control group. According to U.S. Food and Drug Administration, the maximum safe laser power density can be applied to animal bodies is 0.33W/cm^2. Further combining the laser irradiation to perform thermochemotherapy (TCT), the tumors could be completely ablated under the power density of 0.33 W/cm^2 for 20 min (Figure 8A, F). Note that the concentration of CuPPy-NH$_2$ NPs accumulated in the tumor sites is much higher than the injected concentration. So, the power density of 0.33 W/cm^2 is enough. The laser irradiation cause dramatic temperature increments in the local tumor area, and within in 16 min, the central part reaches more than 55 °C. In comparison, for the mice without i.v. injection of NPs, the temperature of tumor area only increases 5 °C. Since the cancerous cells in tumor tissue could usually bear a mild environment below 43 °C, large scales of damaged areas are observed from the H&E stained tumor slices after TCT treatments. The destroyed tumor tissue is not recoverable and in the following 2 months, no tumor recurrence is observed from TCT groups. These evidences confirm that the CuPPy-NH$_2$ NPs are of good tumor theranostic performance.

We also evaluated the biosafety of CuPPy-NH$_2$ NPs. Since CuPPy-NH$_2$ NPs are positive charged, it is capable to assist the tumor accumulation *via* EPR effect. The blood circulation half-life is $t_{1/2}$=1.60 ± 0.3 h by calculating (Figure 7B). This means that the CuPPy-NH$_2$ NPs can be easily captured and removed by mononuclear macrophage system or reticuloendothelium, which avoids the accumulation in the body. After 24 h, the biodistribution of the main organs and tumor are shown in Figure 7c. There is a high value in tumor area. Then, the MRI signal value and the relative MRI signal value of five vital organs and tumor also give the same conclusion revealed in Figure S13. There is a larger response signal in tumor because of the EPR effect. Meanwhile, as shown in Figure S13, there is a high value in the kidney and liver. It proves that NPs mainly exist in the kidney and liver through the circulation of the blood. Besides, the safety of CuPPy-NH$_2$ NPs is further certified by H&E stained. Compared with the control group, the internal organs include heart, liver, spleen, lung and kidneys cannot be fined
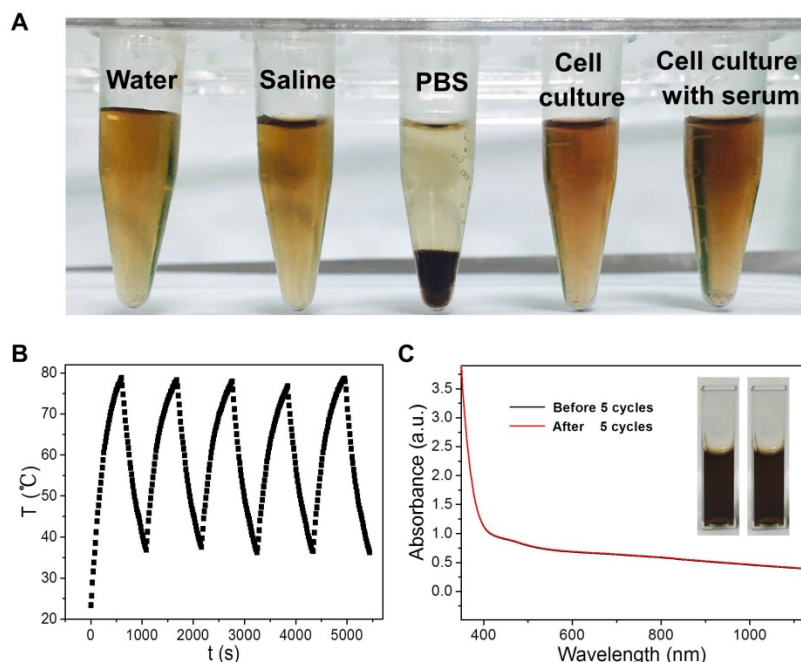

Figure 5. (A) Photographs of CuPPy-NH$_2$ NPs solution after incubation in pure water, saline, PBS, cell culture, and cell culture with 10% serum for 7 days. (B) The real-time temperature records of CuPPy-NH$_2$ NPs solution as heating up and cooling down for 5 cycles at the time interval of 15 s. The laser power density is 4 W/cm^2, and the concentration of CuPPy-NH$_2$ NPs is 1 mg/mL. The absorption spectra of NPs solution before and after 5 cycles are compared in (C).

any changes in the thermo-chemotherapy group (Figure S14). And the weights of the mice of the TCT group are stable (Figure 8B). All of these results indicate that the CuPPy-NH$_2$ NPs are potential safety agents in cancer diagnosis and treatment.
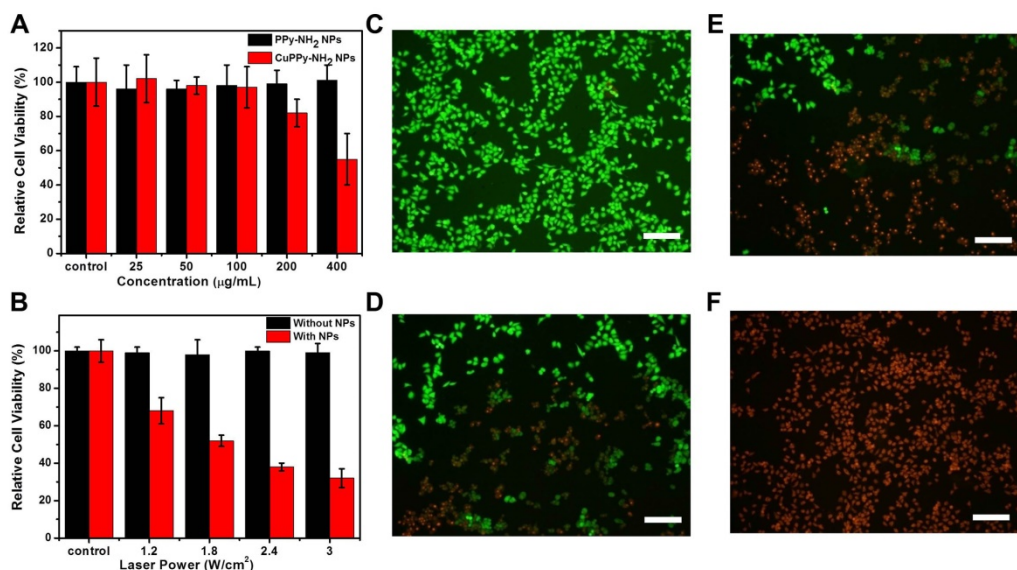

Figure 6. (A) The toxicity test of KB cells with CuPPy-NH$_2$ NPs and PPy-NH$_2$ NPs in different concentration. (B) KB cells are incubated with or without 50 μg/mL CuPPy-NH$_2$ NPs for 2 h, and then they are irradiated by an 808 nm laser with the power density of 1.2, 1.8, 2.4 and 3 W/cm^2 for 8 min. Fluorescent images of PI and FDA co-staining cells after combined therapy for 0 (C), 3 (D), 8 (E), and 10 min (F), respectively. The scale bar in (C-F) represents 50 μm.
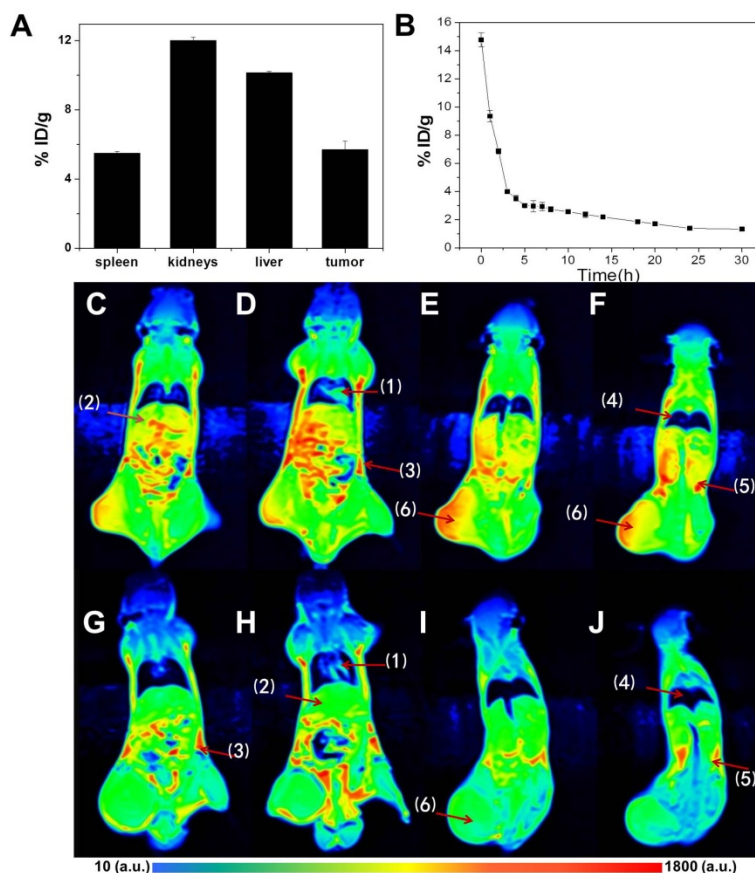

Figure 7. (A) Biodistribution of CuPPy-NH$_2$ NPs in KB-tumor-bearing mice at 24 h i.v. by determining the content of Cu(II) with ICP. (B) Blood circulation of CuPPy-NH$_2$ NPs in KB-tumor-bearing mice at 24 h i.v.. (Figure C-F) The MRI after the injection of NPs. (Figure G-J) The MRI before the injection of NPs. Organs identified by (1)-(6) represent heart, liver, spleen, lungs, kidneys and tumor, respectively. The inset color bar from blue to red represents the MRI signal from low to high.
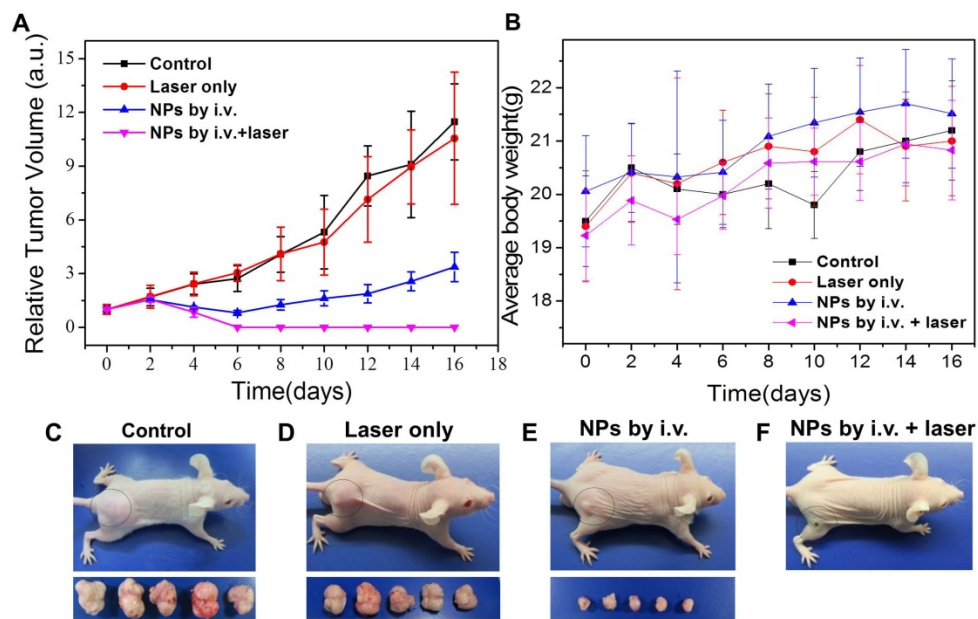
Figure 8. Photothermal therapy of KB tumors *in vivo*. (A) Relative tumor volume growing trend. (B) Average body weight for each group. (C-F) Photographs of typical mouse bearing tumor model and tumors taken from each group in the 16th day. The scale bar in (C-F) represents 20 mm.

Conclusions

In summary, we demonstrate a convenient and efficient fabrication of CuPPy-NH$_2$ NPs with excellent tumor theranostic performance. The CuPPy-NH$_2$ NPs are prepared through oxidation polymerization at room temperature and their function is enriched by the doping of transition metal ions. Due to the strong absorption in the NIR region, CuPPy-NH$_2$ NPs have the function of photothermal therapy. The doped Cu ions also show the potential of chemotherapy. With unpaired electrons in atomic orbits, Cu ions is able to shorten the T$_1$ of protons and light up the target area in T$_1$-weighted imaging. Furthermore, CuPPy-NH$_2$ NPs have good light stability, photothermal stability, biosafety and low toxicity. This kind of transition metal-doped polymer gives a competitive approach for designing and fabricating multimodal theranostic nanoplatforms.

Abbreviations

PPy: Polypyrrole; NPs: nanoparticles; PPy-NH$_2$: Polyaminopyrrole; MRI: magnetic resonance imaging; CuPPy-NH$_2$: Cu(II) and Fe(III) co-loaded polyaminopyrrole; CuPPy: Cu(II) and Fe(III) co-loaded polypyrrole; EPR: enhance permeability and retention; PI: propidium iodide; FDA: fluorescein diacetate; FeCl$_3$·6H$_2$O: Ferric trichloridehexahydrate; CuCl$_2$·2H$_2$O: copper chloride dihydrate; MTT: 3-(4,5-dimethyl-2-thiazolyl)-2,5-diphenyl-2-H-tetrazoliumbromide; MA: mercaptoethylamine; MPA: 3-mercapto-propionic acid; GSH: glutathione; NH$_3$·H$_2$O:

Ammonium hydroxide; -NH$_2$: ammonia; -COOH: sodium citrate; -SH: mercaptoglycerol; ICP-AES: Inductively coupled plasma-atomic emission spectrometry; KB: human oral epithelial carcinoma; OD: optical density; i.v.: intravenous; L: the tumor sizes in long axes; D: the tumor sizes in short axes; H&E: hematoxylin-eosin; UV-vis: UV-visible; TEM: transmission electron microscopy; DLS: dynamic light scattering; IR: infrared ray; XPS: X-ray photoelectron spectroscopy; η: the photothermal transduction efficiency; T$_1$: longitudinal relaxation; r$_1$: respective relaxation rate; NMR: nuclear magnetic resonance; TCT: thermochemotherapy.

Acknowledgments

Supplementary Material

Supplementary figures.
http://www.ntno.org/v02p0211s1.pdf

Competing Interests

The authors have declared that no competing interest exists.

References

1. Wolfbeis O S. An overview of nanoparticles commonly used in fluorescent bioimaging. Chem. Soc. Rev. 2015; 44: 4743-4768.
2. Zhao Z, Fan H, Zhou G, et al. Activatable fluorescence/MRI Bimodal Platform for Tumor Cell Imaging via MnO_2 Nanosheet-Aptamer Nanoprobe. J. Am. Chem. Soc. 2014; 136: 11220-3.
3. Tao W, Zhu X, Yu X, et al. Black Phosphorus Nanosheets as a Robust Delivery Platform for Cancer Theranostics. Adv. Mater. 2017; 29: 1603276-1603284.
4. Qin S Y, Zhang A Q, Cheng S X, et al. Drug self-delivery systems for cancer therapy. Biomaterials. 2017; 112: 234-247.
5. Gobbo O L, Sjaastad K, Radomski M W, et al. Magnetic Nanoparticles in Cancer Theranostics. Theranostics. 2015; 5: 1249-1263.
6. Tang Y, Yang T, Wang Q, et al. Albumin-coordinated assembly of clearable platinum nanodots for photo-induced cancer theranostics. Biomaterials. 2017; 154: 248-260.
7. Goel S, England C G, Chen F, et al. Positron emission tomography and nanotechnology: A dynamic duo for cancer theranostics. Adv. Drug Deliver Rev. 2016; 113: 157-176.
8. Xuan Y, Yang M, Bo P, et al. Gold Nanomaterials at Work in Biomedicine. Chem. Rev. 2015; 115: 10410-10488.
9. Cheng X, Sun R, Yin L, et al. Light-Triggered Assembly of Gold Nanoparticles for Photothermal Therapy and Photoacoustic Imaging of Tumors In Vivo. Adv. Mater. 2017; 29: 1604894-1604900.
10. Liu Y, Yang M, Zhang J, et al. Human Induced Pluripotent Stem Cells for Tumor Targeted Delivery of Gold Nanorods and Enhanced Photothermal Therapy. ACS Nano. 2016; 10: 2375-2385.
11. Chen M, Tang S, Guo Z, et al. Core-shell Pd@Au Nanoplates as Theranostic Agents for In-Vivo Photoacoustic Imaging, CT Imaging, and Photothermal Therapy. Adv. Mater. 2014; 26: 8210-8216.
12. Cheng L, Wang C, Feng L, et al. Functional Nanomaterials for Phototherapies of Cancer. Chem. Rev. 2014; 114: 10869-939.
13. Zheng M, Liu S, Li J, et al. Integrating Oxaliplatin with Highly Luminescent Carbon Dots: An Unprecedented Theranostic Agent for Personalized Medicine. Adv. Mater. 2014; 26: 3554-3560.
14. Li L, Chen C, Liu H, et al. Multifunctional Carbon-Silica Nanocapsules with Gold Core for Synergistic Photothermal and Chemo-Cancer Therapy under the Guidance of Bimodal Imaging. Adv. Funct. Mater. 2016; 26: 4252-4261.
15. Bhattarai P, Dai Z. Cyanine based Nanoprobes for Cancer Theranostics. Adv. Healthcare Mater. 2017; 6: 1700262-1700285.
16. Liang X, Fang L, Li X, et al. Activatable near infrared dye conjugated hyaluronic acid based nanoparticles as a targeted theranostic agent for enhanced fluorescence/CT/photoacoustic imaging guided photothermal therapy. Biomaterials. 2017; 132: 72-84.
17. Liu J, Chen Q, Zhu W, et al. Nanoscale-Coordination-Polymer-Shelled Manganese Dioxide Composite Nanoparticles: A Multistage Redox/pH/H_2O_2-Responsive Cancer Theranostic Nanoplatform. Adv. Funct. Mater. 2017; 27: 1605926-1605937.
18. Liu Q, Song L, Chen S, et al. A superparamagnetic polymersome with extremely high T_2 relaxivity for MRI and cancer-targeted drug delivery. Biomaterials. 2016; 114: 23-33.
19. Yu J, Yin W, Zheng X, et al. Smart MoS_2/Fe_3O_4 Nanotheranostic for Magnetically Targeted Photothermal Therapy Guided by Magnetic Resonance/Photoacoustic Imaging. Theranostics. 2015; 5: 931-945.
20. Li J, Hu Y, Yang J, et al. Hyaluronic acid-modified Fe_3O_4@Au core/shell nanostars for multimodal imaging and photothermal therapy of tumors. Biomaterials. 2015; 38: 10-21.
21. Li Z, Barnes J C, Bosoy A, et al. Mesoporous silica nanoparticles in biomedical applications. Chem. Soc. Rev. 2012; 41: 2590-605.
22. Zhang Z, Wang L, Wang J, et al. Mesoporous Silica-Coated Gold Nanorods as a Light-Mediated Multifunctional Theranostic Platform for Cancer Treatment. Adv. Mater. 2012; 24: 1418-1423.
23. Chen F, Hong H, Zhang Y, et al. In Vivo Tumor Targeting and Image-Guided Drug Delivery with Antibody-Conjugated, Radiolabeled Mesoporous Silica Nanoparticles. ACS Nano. 2013; 7: 9027-9039.
24. Fan W, Shen B, Bu W, et al. A smart upconversion-based mesoporous silica nanotheranostic system for synergetic chemo-/radio-/photodynamic therapy and simultaneous MR/UCL imaging. Biomaterials. 2014; 35: 8992-9002.
25. Zhou M, Zhang R, Huang M, et al. A Chelator-Free Multifunctional [^{64}Cu]CuS Nanoparticle Platform for Simultaneous Micro-PET/CT Imaging and Photothermal Ablation Therapy. J. Am. Chem. Soc. 2010; 132: 15351-8.
26. Wang Z, Huang P, Jacobson O, et al. Biomineralization-Inspired Synthesis of Copper Sulfide-Ferritin Nanocages as Cancer Theranostics. ACS Nano. 2016; 10: 3453-3460.
27. Lv R, Yang P, Hu B, et al. In Situ Growth Strategy to Integrate Up-Conversion Nanoparticles with Ultra-Small CuS for Photothermal Theranostics. ACS Nano. 2017; 11: 1064-1072.
28. Ping H, Qian X, Yu C, et al. Metalloporphyrin-Encapsulated Biodegradable Nanosystems for Highly Efficient Magnetic Resonance Imaging-Guided Sonodynamic Cancer Therapy. J. Am. Chem. Soc. 2017; 139: 1275-1284.
29. Zhou J, Xiong Q, Ma J, et al. Polydopamine-Enabled Approach toward Tailored Plasmonic Nanogapped Nanoparticles: From Nanogap Engineering to Multifunctionality. ACS Nano. 2016; 10: 11066-11075.
30. Wang D, Zhou J, Chen R, et al. Core-Shell Metal-Organic Frameworks as Fe^{2+} Suppliers for Fe^{2+}-Mediated Cancer Therapy under Multimodality Imaging. Chem. Mater. 2017; 29: 3477-3489.
31. Wang Y, Wu B, Yang C, et al. Synthesis and Characterization of Mn:ZnSe/ZnS/ZnMnS Sandwiched QDs for Multimodal Imaging and Theranostic Applications. Small. 2016; 12: 534-546.
32. Yang X, Hong H, Grailer J J, et al. cRGD-functionalized, DOX-conjugated, and ^{64}Cu-labeled superparamagnetic iron oxide nanoparticles for targeted anticancer drug delivery and PET/MR imaging. Biomaterials. 2011; 32: 4151-4160.
33. Zeng J, Cheng M, Wang Y, et al. pH-Responsive Fe(III)-Gallic Acid Nanoparticles for In Vivo Photoacoustic-Imaging-Guided Photothermal Therapy. Adv. Healthcare Mater. 2016; 5: 772-780.
34. Liu X L, Ng C T, Chandrasekharan P, et al. Synthesis of Ferromagnetic $Fe_{0.6}Mn_{0.4}O$ Nanoflowers as a New Class of Magnetic Theranostic Platform for In Vivo T_1-T_2 Dual-Mode Magnetic Resonance Imaging and Magnetic Hyperthermia Therapy. Adv. Healthcare Mater. 2016; 5: 2092-2104.
35. Verwilst P, Park S, Yoon B, et al. Recent advances in Gd-chelate based bimodal optical/MRI contrast agents. Chem. Soc. Rev. 2015; 44: 1791-806.
36. Feng C, Bu W, Zhang S, et al. Gd^{3+}-Ion-Doped Upconversion Nanoprobes: Relaxivity Mechanism Probing and Sensitivity Optimization. Adv. Funct. Mater. 2013; 23: 298-307.
37. Siddiqui M M, Raisbahrami S, Turkbey B, et al. Comparison of MR/Ultrasound Fusion-Guided Biopsy With Ultrasound-Guided Biopsy for the Diagnosis of Prostate Cancer. Jama. 2015; 313: 390-397.
38. Dimopoulos M A., Hillengass J, Usmani S. Role of Magnetic Resonance Imaging in the Management of Patients With Multiple Myeloma: A Consensus Statement. J. Clin. Oncol. 2015; 33: 657-664.
39. Lin M, Wang D, Li S, et al. Cu(II) doped polyaniline nanoshuttles for multimodal tumor diagnosis and therapy. Biomaterials. 2016; 104: 213-222.
40. Yang G, Gong H, Liu T, et al. Two-dimensional magnetic WS_2@Fe_3O_4 nanocomposite with mesoporous silica coating for drug delivery and imaging-guided therapy of cancer. Biomaterials. 2015; 60: 62-71.
41. Anthony L, Cacoub P, Macdougall I C, et al. Iron deficiency anaemia. Lancet. 2016; 387: 907-916.
42. Gubler C J, Lahey M E, Cartwright G E, et al. Studies on Copper Metabolism. IX. the Transportation of Copper in Blood. J. Clin. Invest. 1953. 199: 405-414.
43. Zhang F L, Song M R, Yuan G K, et al. A Molecular Combination of Zinc(II) Phthalocyanine and Tamoxifen Derivative for Dual Targeting Photodynamic Therapy and Hormone Therapy. J. Med. Chem. 2017; 60: 6693-6703.
44. Shahnaz R, Nazem G, Mardani M, et al. Co-Transplantation of Human Neurotrophic Factor Secreting Cells and Adipose-Derived Stem Cells in Rat Model of Multiple Sclerosis. Cell J. 2018; 1: 46-52.
45. Zhang P, He Z, Wang C, et al. In Situ Amplification of Intracellular MicroRNA with MNAzyme Nanodevices for Multiplexed Imaging, Logic Operation, and Controlled Drug Release. ACS Nano. 2015; 9: 789-798.
46. Nel A, Xia T, Mädler L, et al. Toxic potential of materials at the nanolevel. Science. 2006; 311: 622-627.
47. Zhao L, Peng J, Huang Q, Near-Infrared Photoregulated Drug Release in Living Tumor Tissue via Yolk-Shell Upconversion Nanocages. Adv. Funct. Mater. 2014; 24: 363-371.
48. Yang K, Xu H, Cheng L, et al. In Vitro and In Vivo Near-infrared Photothermal Therapy of Cancer Using Polypyrrole Organic Nanoparticles. Adv. Mater. 2012; 24: 5586-92.
49. Chen M, Fang X, Tang S, et al. Polypyrrole nanoparticles for high-performance in vivo near-infrared photothermal cancer therapy. Chem. Commun. 2012; 48: 8934-6.
50. Yang S, Li Z, Wang Y, et al. Multifunctional Bi@PPy-PEG Core-Shell Nanohybrids for Dual-Modal Imaging and Photothermal Therapy. ACS Appl. Mater. Interfaces. 2018; 10: 1605-1615.
51. Liu Y, Yang X, Huang Z, et al. Magneto-Plasmonic Janus Vesicles for Magnetic Field-Enhanced Photoacoustic and Magnetic Resonance Imaging of Tumors. Angew. Chem. Int. Ed. 2016; 55: 15297-15300.
52. Li Y, Tang J, He L, et al. Core-Shell Upconversion Nanoparticle@Metal-Organic Framework Nanoprobes for Luminescent/Magnetic Dual-Mode Targeted Imaging. Adv. Mater. 2015; 27: 4075-4080.
53. Chen Y, Ai K, Liu J, et al. Polydopamine-based coordination nanocomplex for T_1/T_2 dual mode magnetic resonance imaging-guided chemo-photothermal synergistic therapy. Biomaterials. 2015; 77: 198-206.
54. Yavuz M S, Cheng Y, Chen J, et al. Gold nanocages covered by smart polymers for controlled release with near-infrared light. Nat. Mater. 2009; 8: 935-939.
55. Huang X, Tang S, Liu B, et al. Enhancing the Photothermal Stability of Plasmonic Metal Nanoplates by a Core-Shell Architecture. Adv. Mater. 2011; 23: 3420-5.
56. Kim S E, Zhang L, Ma K, et al. Ultrasmall nanoparticles induce ferroptosis in nutrient-deprived cancer cells and suppress tumour growth. Nat Nanotechnol. 2016; 11: 977–985.
57. Shaffer T M, Harmsen S, Khwaja E, et al. Stable Radiolabeling of Sulfur-Functionalized Silica Nanoparticles with Copper-64. Nano Letters. 2016; 16: 5601-5604.
58. Ellison P A, Feng C, Goel S, et al. Intrinsic and Stable Conjugation of Thiolated Mesoporous Silica Nanoparticles with Radioarsenic. ACS Appl. Mater. Interfaces. 2017. 9: 6772-6781.

59. Zhang Z, Xiong Z, Tao Z, et al. Structural study of compartmental complexes of europium and copper. J. Mol. Struct. 1999; 478: 23-27.

60. Dake L S, King D E, Czanderna A W. Ion scattering and X-ray photoelectron spectroscopy of copper overlayers vacuum deposited onto mercaptohexadecanoic acid self-assembled monolayers. Solid State Sci. 2000; 2: 781-789.

61. Willett R D, Jr C D, Kruh R F, et al. Crystal Structures of KCuCl3 and NH4CuCl3. J. Chem. Phys. 1963; 38: 2429-2436.

62. Bass L A, Mu W, And M J W, et al. In Vivo Transchelation of Copper-64 from TETA-Octreotide to Superoxide Dismutase in Rat Liver. Bioconjugate Chem. 2000. 11: 527-532.

63. Boswell C A, Sun X, Niu W, et al. Comparative in vivo stability of copper-64-labeled cross-bridged and conventional tetraazamacrocyclic complexes. J. Med. Chem. 2004. 47: 1465-1474.